

Research Article

On Synergistic Integration of Adaptive Dithering Based Internal Model Control for Hysteresis Compensation in Piezoactuated Nanopositioner

Saikat Kumar Shome,¹ Mangal Prakash,² Sourav Pradhan,² and Arpita Mukherjee¹

¹Electronics & Instrumentation Group, CSIR-CMERI, Durgapur 713209, India

²Department of Electrical Engineering, University of Minnesota, Minneapolis, MN 55455, USA

Correspondence should be addressed to Saikat Kumar Shome; saikatkuarshome@gmail.com

Received 17 September 2014; Accepted 1 December 2014

Academic Editor: Xinggang Yan

Copyright © 2015 Saikat Kumar Shome et al. This is an open access article distributed under the Creative Commons Attribution License, which permits unrestricted use, distribution, and reproduction in any medium, provided the original work is properly cited.

Piezoelectric-stack actuated platforms are very popular in the parlance of nanopositioning with myriad applications like micro/nanofactory, atomic force microscopy, scanning probe microscopy, wafer design, biological cell manipulation, and so forth. Motivated by the necessity to improve trajectory tracking in such applications, this paper addresses the problem of rate dependent hysteretic nonlinearity in piezoelectric actuators (PEA). The classical second order Dahl model for hysteresis encapsulation is introduced first, followed by the identification of parameters through particle swarm optimization. A novel inversion based feedforward mechanism in combination with a feedback compensator is proposed to achieve high-precision tracking wherein the paradoxical concept of noise as a performance enhancer is introduced in the realm of PZAs. Having observed that dither induced stochastic resonance in the presence of periodic forcing reduces tracking error, dither capability is further explored in conjunction with a novel output harmonics based adaptive control scheme. The proposed adaptive controller is then augmented with an internal model control based approach to impart robustness against parametric variations and external disturbances. The proposed control law has been employed to track multifrequency signals with consistent compensation of rate dependent hysteresis of the PEA. The results indicate a greatly improved positioning accuracy along with considerable robustness achieved with the proposed integrated approach even for dual axis tracking applications.

1. Introduction

Precision positioning applications are ubiquitous in engineering and industrial applications, arising with rapid expansion of nanoscale technologies [1, 2]. Many system applications demand positioning control accuracies down to nanometer resolution. Of late, piezoelectric actuators (PZAs) have dominated the field of precision positioning and have emerged as the most popular class of actuators in this domain. The success of PZAs can be attributed to their high resolution, high electromechanical coupling efficiency, fast frequency response, high stiffness, and small thermal expansion during actuation. Dynamically interactive micro/nanomanipulation applications typically require control actuators that are not

only capable of providing accurate reference tracking but also yield robust stable force control [3–5]. These objectives are severely hampered by many inherent nonlinearities like hysteresis, creep, vibrations, and so forth, the effects of which are exaggerated at small scales. Of these, hysteresis affects the precision pointing capabilities the most. Hysteresis is known to have a destabilizing effect in addition to introducing severe positioning inaccuracies, limit cycles, and chattering [6]. Another important issue related to the control of piezoelectric-material actuated positioning platform is that the system dynamics can vary with environmental and loading conditions. This necessitates the urgency to develop efficient control structures for PZAs in order to keep up with their increasingly demanding design requirements.

The application of electric field to ferroelectric PZAs causes them to exhibit intrinsic hysteretic behavior [7]. Controlling the induced charge is an effective way to mitigate hysteresis but this method is hugely expensive for the requirement of costly materials for charge measurement and amplification. Besides, the accuracy and responsiveness of the actuator is significantly compromised with this method. An extensive amount of research has been invested into implementation of different control structures to accommodate piezoelectric hysteresis and other nonlinearities.

Classical controllers like PI and PID have been shown to possess limited bandwidth and, hence, are effective with only systems having minimal hysteresis. As the piezohysteresis increases, control gains need to be increased for desired accuracy. However, this method is not effective as large controller gains tend to destabilize the system. Application of linear robust techniques like $H-\infty$ control has been successfully implemented to augment system bandwidth and robustness to hysteresis and nonlinearities [8, 9]. However, such methods focus centrally on compensating intrinsic nonlinearities and the issue of rejecting effects of external disturbances and parametric variations is given a secondary treatment. Control designs using nonlinear inverse filters have also been employed in practice to approximately linearize the material response. Such an approach allows the implementation of linear control techniques to the newly linearized plant [10, 11]. Sliding mode control (SMC) strategy has been pitched in as an effective nonlinear control strategy [12–16]. However, it is a well-known fact that chattering phenomenon in SMC renders it impractical [17]. Elmali and Olgac proposed a sliding mode controller with perturbation estimation to overcome the drawbacks of conventional SMC [18]. Discrete time SMC has been proposed in [19–21] to realize SMC on sampled data system. Bashash and Jalili have proposed a Lyapunov based robust adaptive controller for simultaneous tracking of a double axis piezoflexural stage [2]. In order to address the uncertainty in hysteresis, adaptive controls like model reference adaptive control (MRAC) have been investigated in [22, 23] but these methods suffer from either overparameterization or need for slow adaptation. Broadly, all the control strategies can be classified under two major groups: feedforward and feedback. Feedforward schemes essentially have an inverse hysteresis model to compensate for hysteretic nonlinearity [24–26]. High sensitivity to modeling errors and plant parametric uncertainties, however, demand the application of feedback controller. Feedback techniques improve the bandwidth of feedforward controllers and thus improve system response [27].

Amidst the wide spectrum of control techniques available in the gamut of nan positioning, it becomes difficult to select a particular controller. In this work, the authors have attempted to present a logical framework for the design of controllers for nan positioning. The primary requirement of any control technique is that it should possess a sound fundamental basis in addition to being simple to understand and implement. Internal model control (IMC) is known to be a suitable framework which satisfies these basic objectives [28, 29]. Unlike most other controllers, the complexity of IMC has an explicit dependence on two factors: model

complexity and the desired performance requirements. This allows for a logical controller design where robustness and control quality can be directly manipulated according to the designer's requirements. Besides, transparency, tractability, and intuitive appeal associated with IMC makes it germane for industrial applications like control for position tracking of permanent-magnet synchronous motor servo system [30]. The authors have explored the capabilities of IMC in this work in the gamut of nan positioning with piezoactuator. This has been a relatively pristine area for the application of IMC till date.

The implementation of any control strategy is dependent upon the choice of a reasonable model structure. Many model frameworks are available in the literature which can encapsulate the system behavior to different degrees. These frameworks not only provide a general insight into PZA behavior but also present specific mathematical formulations for model based control system and design. Numerous hysteresis models are available in the literature of which Preisach model, Dahl model, Bouc-Wen model, Maxwell model, Prandtl-Ishlinskii model, and so forth are the most popular ones. Inverse Preisach model is used in [31] to design a cascaded proportional-derivative/lead-lag feedback controller. A modified Prandtl-Ishlinskii model combined with SMC is presented in [32, 33] whereas a hysteresis observer based Bouc-Wen model is proposed in [34] for hysteretic linearization. The purpose of these models is to map the dynamics of the system in a manner that is applicable over a wide range of operating condition.

Shome et al. have spawned a new dimension to the control of PZA based on the concept of dither induced stochastic resonance [35, 36]. Contrary to the generic notion, an externally added high frequency noise has been seen to alleviate hysteretic nonlinearity with amazing effectiveness. In technical terms, such a deliberately added noise is called dither. The physics behind dithering can be understood by correlating it with another phenomenon known as stochastic resonance (SR). Using the motion tracking error as a measure of system performance, the signature of SR is a pronounced dip in tracking error followed by a gradual increase as the noise intensity is changed. SR demands three basic ingredients: (a) a nonlinear system, (b) a subthreshold periodic signal, and (c) noise. Dither based control of PZA meets all these requirements and, hence, SR is observed in terms of reduced tracking error.

1.1. Objectives. This work focuses on enhancing the motion tracking performance of an industry-grade biaxial (X - Y) piezoelectric-stack actuator. In this paper, inversion-based feedforward technique is combined with a feedback controller to utilize the advantages of both feedforward and feedback simultaneously. Plant dynamics are captured with a second order Dahl model. This model has been established to be better than a Bouc-Wen model of the same order in representing the asymmetric hysteresis loops [37]. Moreover, a second order Dahl model has lesser number of parameters and hence it is easier to implement as compared to other higher order Dahl models. The implementation of inverse

Dahl model in the feedforward path eliminates the need of developing a separate velocity observer which can be cumbersome at times.

The proposition of useful noise has been established with SR manifesting its existence in the realm of PZAs. SR is already known to compensate for hysteresis nonlinearity quite amazingly [35, 36]. To exploit the capabilities of dither based control in real-time, it is necessary to implement the controller in an adaptive manner. The possibility of unstructured uncertainties and uncertain dynamics and modeling mismatch cannot be negated practical circumstances. An adaptive approach aims at imparting robustness to the system against external disturbances and parametric uncertainties. The concept of dither based control has been extended to yield a novel adaptive control scheme called FFT adaptive loop control. However, adaptive control approach relies heavily on the foreknowledge of the trajectory being tracked. To overcome this, an internal model based control (IMC) structure has been augmented with FFT adaptive loop control. The proposed novel amalgamation of adaptive dithering and IMC adds extra robustness to the system against endogenous and exogenous variations.

The control design is verified on a commercially available nanopositioning stage manufactured by Physik Instrumente. The performance of the proposed controller is tested for sinusoidal motion tracking with low frequency inputs and a comparison is drawn out with the existing feedforward cum PID based feedback approach. Tracking results for multiamplitude, multifrequency signals are also presented to demonstrate the control efficacy against variations in input. Circular contour tracking test is then performed to verify the controller ability to track complex 2D trajectories. Since robustness behavior against external disturbances and parametric variations is important in practical applications, the proposed controller is tested for varying intensities of noise and with plant parameters fluctuating in range of 0–2% of nominal value.

This work focuses on devising suitable control structures for adaptive hysteresis compensation of a commercial piezoelectric actuator. A novel dither based scheme is presented which implicitly captures the relationship between nonlinear hysteresis and dither dosage and adaptively modifies dither inoculation by resorting to a harmonic analysis of system output. This methodology is coined as FFT adaptive scheme in this work. Despite the suitability of IMC as a simple, tractable, and robust control framework, it has received scant attention in the ambit of nanopositioning till date to the best of the knowledge of the authors. The highlight of this work is combination of IMC with adaptive dither approach to extract the benefits of adaptive and robust approach together. The efficacy of the proposed cumulative approach has been verified in this research by investigations on a two-axis stack actuated piezopositioning platform.

1.2. Organization. A mathematical formulation of the PZA in presence of hysteretic nonlinearity is presented in Section 2. Section 3 gives details of the implemented control strategies. Reference motion tracking results with the proposed controllers is presented in Section 4 to show the improvement

in system performance with the proposed control structures. Section 5 concludes the paper.

2. Procedure for Dynamic Modeling and System Identification

2.1. Dynamic Modeling. Piezoflexural stages are designed to provide multiple axis motions with micro/nanometric resolution for a wide range of displacements. Several piezoelectric-stack actuators are coupled to a flexural mechanism to provide multiple-axis motion for a single moving stage. In this work, a biaxial nanopositioning stage capable of delivering motion along x - and y -axes is considered. Two separate single-input single-output (SISO) manipulators are used for this purpose, each catering to the positioning demand along a single axis. For the sake of brevity, the modeling of only one such manipulator along x axis is undertaken here. The procedure for the equivalent modeling of the system has been borrowed from [37]. Considering the mechanical parts of micromanipulator system to be linear and of second order, the dynamic model of the system in presence of nonlinear hysteresis is given by

$$M\ddot{x} + D\dot{x} + Kx = Tu - F_h, \quad (1)$$

where the parameters x , K , D , and M represent the x -axis displacement, stiffness, damping coefficient, and equivalent mass of the XY micromanipulator, respectively. T denotes the piezoelectric coefficient, u stands for the input voltage, and F_h indicates the hysteretic effect in terms of force. In state space form, second order Dahl model based manipulator in hysteretic environment is represented by [38]

$$\dot{V} = A_h V \dot{x} + B_h u_p \dot{x}, \quad (2)$$

$$F_h = C_h V, \quad (3)$$

where u_p is a constant (set to 30), $V = [q_1 \ q_2]^T$ is the intermediate state vector, and

$$A_h = \begin{bmatrix} 0 & 1 \\ -a_2 & -\text{sgn}(\dot{x}) a_1 \end{bmatrix}, \quad (4)$$

$$B_h = \begin{bmatrix} 0 \\ 1 \end{bmatrix},$$

$$C_h = [b_1 \ \text{sgn}(\dot{x}) b_0].$$

The hysteretic parameters are calculated using the following relations:

$$a_1 = \frac{2}{T_d} \ln \frac{P_{n-1} - P_s}{P_n - P_s},$$

$$a_2 = \frac{4\pi^2}{T_d^2} + \frac{a_1^2}{4}, \quad (5)$$

$$b_1 = G_{dc} a_2,$$

$$b_0 = S_0,$$

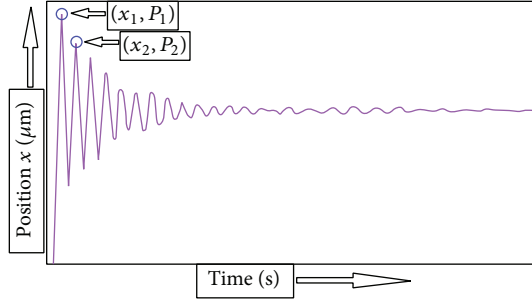


FIGURE 1: Open loop time domain step response for a piezoelectric actuator.

where T_d is the time period of the damped oscillations of time response of the system which is equal to $x_2 - x_1$ from Figure 1. P_n is the overshoot of the n th peak and P_s is the steady state response. G_{dc} represents the initial gain and S_0 is the initial slope of the response.

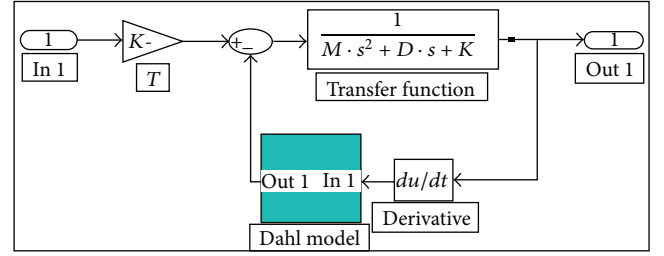
2.2. System Identification. The open loop time domain step response of the employed system is generalized in Figure 1. The nonlinearity introduced by hysteresis makes system identification by conventional methods a difficult task. Since the hysteretic parameters have already been identified by the step response test, only the dynamic parameters M , D , K , and T need to be identified. These parameters can be identified simultaneously by swarm intelligence techniques like particle swarm optimization (PSO). It has been observed that Dahl model is more sensitive to changes in dynamic parameters and hardly exhibits much sensitivity for changes in hysteretic parameters. The choice of dynamic parameters, thus, assumes an even greater significance. PSO is used in this work due to its superiority over other optimization algorithms like genetic algorithm and direct search approach [39, 40].

The choice of fitness function and bounds on the variables to be optimized is an equally important issue while using PSO. In this study, the fitness function is chosen as follows:

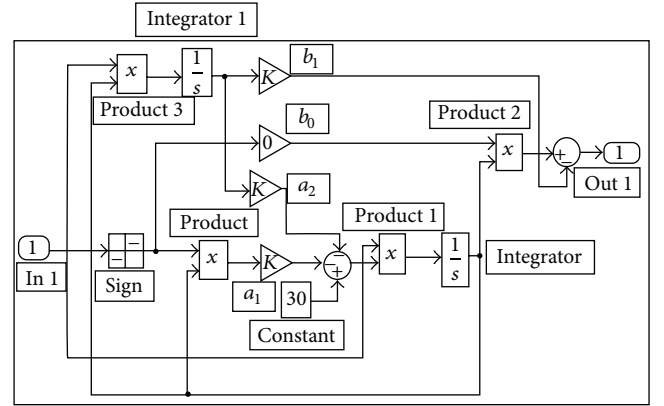
$$g(M, D, K, T) = \sqrt{\frac{1}{c} \sum_{i=1}^c E_i^2}, \quad (6)$$

with $E_i = x_i - x'_i$,

where c denotes the total number of samples, E_i is the error of the i th sample, x_i is the experimental result, and x'_i is the Dahl model output. The search space assigned with each variable is constrained within the following ranges: $M \in [0.01, 0.05]$, $D \in [10, 20]$, $K \in [1 \times 10^7, 5 \times 10^7]$, and $T \in [0.005, 0.02]$. The model identification process through PSO is an offline process. With a full range of input voltage (0–75 V) impressed upon the PZA, the response (output displacement) is recorded. The dynamic model with Dahl model hysteresis is realized in LABVIEW as illustrated in Figures 2(a) and 2(b). Through simulation, the model output is generated for the same input voltage. Finally, PSO is employed to obtain optimum values of model parameters in order to match simulation results with the experimental data.



(a)



(b)

FIGURE 2: (a) System floor plan of the plant using Dahl model; (b) Dahl model for calculating the hysteretic term F_h .

3. Control Design

In this section, the design procedure of inversion based feedforward control and its augmentation with a feedback controller is discussed in detail. A novel adaptive control structure follows which harnesses the capability of dither induced SR. This scheme is then integrated with internal model control (IMC) to achieve increased tracking robustness in presence of external disturbances and plant parametric uncertainties.

3.1. Inversion Based Feedforward Controller. The goal of the inversion based controller is to find the input u that when fed to the system with known dynamics $H(s)$ produces the desired output x_d , that is,

$$X_d(s) = H(s)U(s), \quad (7)$$

where $U(s)$ and $X_d(s)$ are Laplace Transforms of u and x_d , respectively. The PZA is modeled as the cascade of dynamic model and the inverse model as shown in Figure 3, in which the desired trajectory x passes through the inverse hysteresis submodel, and its output u is the compensated voltage supplied to the subsequent plant model to generate the desired displacement x_d . However, this technique has two major downsides:

- (1) the controller remains susceptible to load side fluctuations;

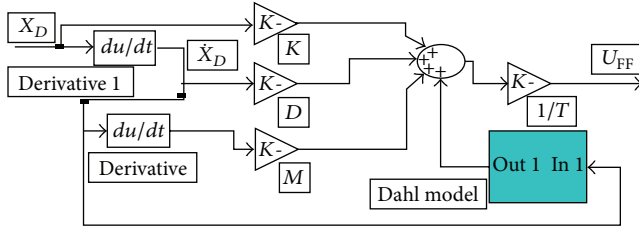


FIGURE 3: Inverse Dahl model for compensated voltage calculation.

- (2) the construction of the compensated voltage u is dependent on the accuracy of the inverse model.

But in practice due to ambient noise, limitations on machine precision and other exogenous variables unaccounted for, it is difficult to identify the system accurately. Modeling errors can be reduced by using higher order models but it introduces unnecessary complications in controller design. An alternate to this is to use a feedback controller in conjunction with a feedforward control scheme.

3.2. Feedforward Cum Feedback Compensation. As mentioned earlier, inversion based feedforward compensator alone cannot account for model imperfections and other system disturbances. However, a feedforward compensator when augmented with a feedback controller can take care of such imperfections. The schematic of feedforward cum feedback controller is illustrated in Figure 4. The feedback controller involves a PID compensator which takes in the error as its input. Mathematically, the control inputs generated by the feedforward and feedback compensators are given by (8) and (9), respectively. The overall control signal can be calculated by (10). Consider the following:

$$u_{ff} = \frac{1}{T} (M\ddot{x} + D\dot{x} + Kx + F_h), \quad (8)$$

$$u_{fb} = K_p \left[e(t) + \frac{1}{T_i} \int_0^T e(t) + T_d \frac{d}{dt} e(t) \right], \quad (9)$$

$$u(t_k) = u_{ff}(t_k) + u_{fb}(t_k), \quad (10)$$

where K_p is proportional gain, T_i is integral time, T_d is derivative time, and $e(t) = x_d(t) - x(t)$. The values of proportional (P), integral (I), and derivative (D) gains used for the controller are 0.12, 13.33, and 0, respectively.

3.3. Unadaptive Dither Based Hysteresis Compensation. Dithering has been a very popular technique for improving performance of digitizing systems. Dither applications were initially restricted to audio and video areas but nowadays its usage has spanned over different areas. Recently, cross effects between dithering and hysteresis in piezoelectric-stack actuators have been analyzed in the literature [35, 36, 41, 42]. Dithering can be defined as adding some noise to a system/signal to linearize its characteristics. Usually, dither inputs are high frequency noise signals. Dithering has indeed the effect of smoothing the effects of hysteresis in PZAs, thanks to the exhibition of dither induced SR.

Highly nonlinear models having a threshold show an interesting behavior when acted upon by noisy signals (dither). Dynamical models like neuron firing, avalanches, analog to digital converters, and laser systems fall under this category [43]. PZAs fall under the same category of systems having high nonlinearity due to hysteresis. The study of input-output characteristics of PZA in the presence of a small periodic signal embedded in a noisy background reveals that when the noise intensity matches a specific value, the tracking error reaches a minimum. The cooperation between a periodic signal and stochastic signal (noise) leading to a peak in signal-to-noise ratio (SNR) is considered the thumbprint of SR.

3.3.1. General Overview of SR. The physical ideas of SR can be elucidated in the context of bistable system in a symmetrical double well potential [44]. Consider a heavily damped particle of mass m and viscous friction γ moving in a symmetric double well potential given by (11). Fluctuational forces like those induced by coupling to a heat bath cause the particle to make transitions between the neighboring potential wells with Kramers rate given by (13) where ω_o and ω_b are the angular frequencies at the minima of potential well and at the top of potential barrier, respectively, and D is the noise strength. In the presence of a weak periodic forcing like $A_0 \cos(\Omega t)$, the potential well is successively raised and lowered thereby asymmetrically tilting it as shown in Figures 5(a) and 5(b). The periodic forcing causes the potential well to tilt asymmetrically up and down on a periodic basis. Though the periodic forcing is too weak to let the particle roll from one well to another in a periodic fashion, the particle's noise induced hopping can become synchronized with the periodic forcing. This situation is called stochastic resonance in the double well potential. Statistically, stochastic resonance is observed when the average waiting time $T_k(D)$ between two noise induced interwell transitions is comparable to half the period T_Ω of the periodic forcing. Mathematically, the time scale matching condition for SR is described by (15). This condition is called SR and its manifestation for the symmetric double-well potential is illustrated in Figure 5(b):

$$V(x) = \frac{1}{4}bx^4 - \frac{1}{2}ax^2, \quad (11)$$

$$\Delta V = \frac{a^2}{4b}, \quad (12)$$

$$x_m = \sqrt{\frac{a}{b}},$$

$$r_k = \frac{\omega_o \omega_b}{2\pi\gamma} \exp\left(-\frac{\Delta V}{D}\right), \quad (13)$$

$$\omega_o^2 = V'' \frac{x_m}{m}, \quad (14)$$

$$\omega_b^2 = V'' \frac{x_b}{m},$$

$$2T_k = T_\Omega. \quad (15)$$

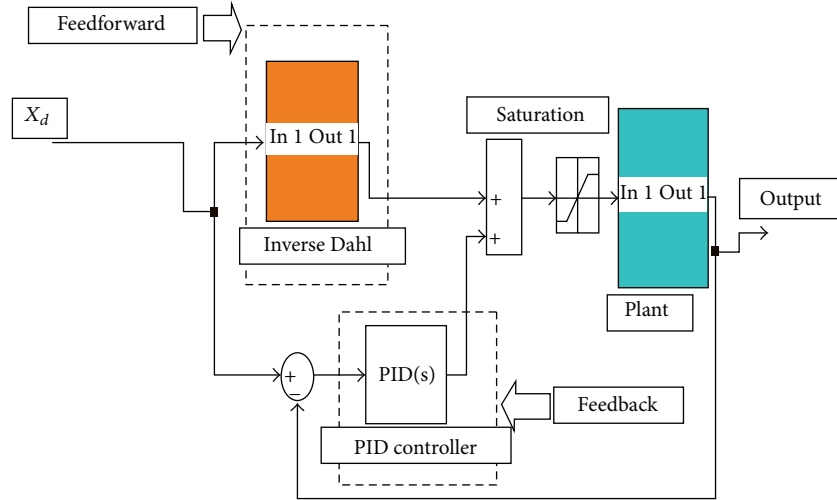


FIGURE 4: Pure cascaded feedforward cum feedback control strategy.

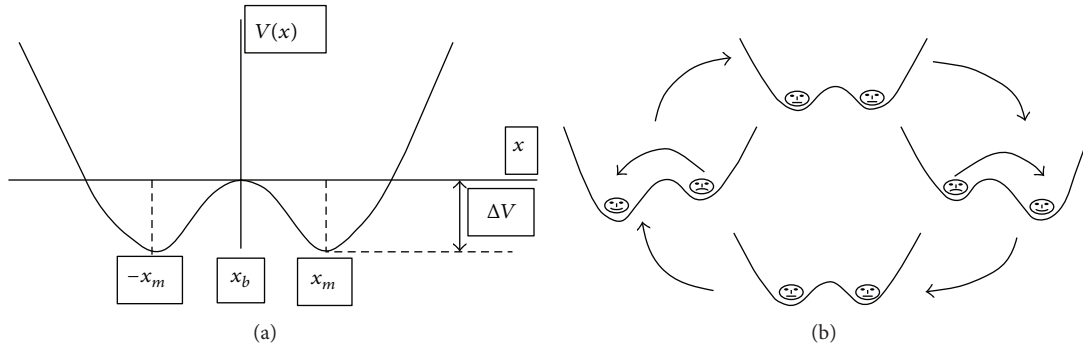


FIGURE 5: (a) Double-well potential function; (b) synchronized hopping of the particle with periodic input in presence of a certain amount of noise.

3.3.2. SR in Bistable Systems with Asymmetric Potential. The basic overview of SR for systems modeled by a symmetric bistable potential provides the required insight for analyzing systems represented by asymmetric bistable potential. Piezoelectric-stack actuated platform can be modeled as a bistable system with unsymmetrical potential function. SR has been investigated in this subsection with focus on bistable systems with asymmetric potential [45].

Consider a particle of unity mass and damping factor ζ moving in an asymmetric double well potential V acted upon by a sinusoid with amplitude A_o and white noise $\sigma\psi$. The dynamics of the particle is given by

$$\begin{aligned} \dot{x} &= v, \\ v &= -V'(x) - \zeta v + \sigma\psi(t) + A_o \cos(\Omega_o t), \end{aligned} \quad (16)$$

where x and v represent the position and velocity of particle, respectively, and σ is the standard deviation of white noise. The potential function is assumed to have a local minima at $x = x_L$ and at $x = x_R$ while the maximum is located at $x = x_M$ such that $x_R < x_M < x_L$. In the following analysis, the variables in the left well are denoted by L and those in the right well are denoted by R .

Starting with an unmodulated system, that is, $A_o = 0$, and assuming an initial position $x = x_o$ at time $t = t_o$, the autocorrelation of random variable $x(t)$ can be computed based on the conditional probability density $p(x, t) = p(x, t | x_o, t_o)$. The unmodulated transition rate represented by $r(x_o)$ is defined as the inverse of the average time taken by the particle to cross the potential hill at $x = x_M$. For large damping (up to errors of order ζ^{-2}), the transition rates are roughly given by

$$\begin{aligned} r_L &= \frac{[1 + \zeta^{-2} V''(x_M)] [|V''(x_M)| V''(x_L)]^{0.5}}{2\pi\zeta} e^{-2\zeta V_L/\sigma^2}, \\ r_R &= \frac{[1 + \zeta^{-2} V''(x_M)] [|V''(x_M)| V''(x_R)]^{0.5}}{2\pi\zeta} e^{-2\zeta V_R/\sigma^2}, \end{aligned} \quad (17)$$

where

$$V_L = V(x_M) - V(x_L), \quad V_R = V(x_M) - V(x_R). \quad (18)$$

The time varying potential function is defined as

$$\widehat{V}(x, t) = V(x) - V(x_M) - A_o(x - x_L - \chi) \cos(\Omega_o t), \quad (19)$$

$$\text{where } \chi = \frac{x_R - x_L}{2}. \quad (20)$$

Using (18) and (19), the time varying potential functions for the left and right halves are given as

$$\widehat{V}(x_L, t) = -V_L + A_o \chi \cos(\Omega_o t), \quad (21)$$

$$\widehat{V}(x_R, t) = -V_R - A_o \chi \cos(\Omega_o t).$$

If $A_o \chi \ll \min(V_L, V_R)$, x_L and x_R can still be considered as the minima on the potential well. The modulated transition rates can be calculated similar to (17). The modulated transition rates when computed take the form of (22). Consider the following:

$$\mu_L(t) = r_L \cdot e^{2\lambda \cos(\Omega_o t)}, \quad (22)$$

$$\mu_R(t) = r_R \cdot e^{-2\lambda \cos(\Omega_o t)},$$

$$\text{where } \lambda = \frac{\chi A_o \zeta}{\sigma^2}. \quad (23)$$

Up to errors of orders $O(\lambda^2)$, (22) can be reduced to

$$\mu_L(t) = r_L \cdot [1 + 2\lambda \cos(\Omega_o t) + 2\lambda^2 \cos^2(\Omega_o t)], \quad (24)$$

$$\mu_R(t) = r_R \cdot [1 - 2\lambda \cos(\Omega_o t) + 2\lambda^2 \cos^2(\Omega_o t)].$$

The rate equation given by (25) determines the probability P_r of locating the particle on either side of the potential hill:

$$\frac{dP_r}{dt} = -\frac{dP_L}{dt} = \mu_L(t) P_L - \mu_R(t) P_R. \quad (25)$$

Since $P_L + P_R = 1$, (25) can be modified as

$$\frac{dP_r}{dt} = \mu_L(t) - [\mu_R(t) + \mu_L(t)] P_R. \quad (26)$$

On substituting (24) in (26) and neglecting higher order terms, we have

$$\begin{aligned} \frac{dP_r}{dt} &= r_L [1 + 2\lambda \cos(\Omega_o t) + 2\lambda^2 \cos^2(\Omega_o t)] \\ &- [2r + 2\rho\lambda \cos(\Omega_o t) + 4r\lambda^2 \cos^2(\Omega_o t)] P_R, \end{aligned} \quad (27)$$

where

$$r = \frac{r_L + r_R}{2}, \quad \rho = r_L - r_R. \quad (28)$$

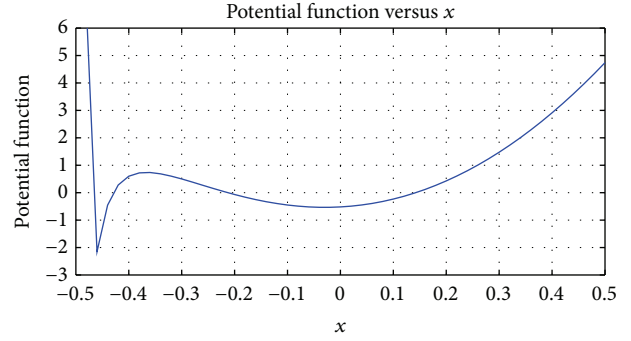


FIGURE 6: Plot of potential function versus x .

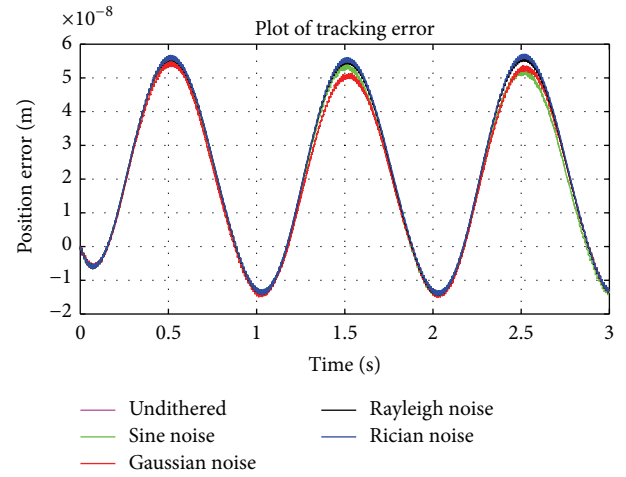


FIGURE 7: Tracking error plots for various noises.

The solution of ODE (27) can be generated to yield the conditional probability of finding the particle in the right potential well.

Equation (29) represents a new stochastic variable which is generated to find the autocorrelation of particle position $x(t)$:

$$y = f(x) = \begin{cases} 0, & x < x_m \\ 2\chi, & x > x_m. \end{cases} \quad (29)$$

The probability density of y is given by

$$p(y, t) = P_R(t) \delta(y - 2\chi) + P_L(t) \delta(y). \quad (30)$$

The autocorrelation function computed by (29) is defined as

$$\begin{aligned} E[y(t + \tau) y(t) | y_o, t_o] \\ = (2\chi)^2 P_R(t + \tau | 2\chi, t) P_R(t | y_o, t_o). \end{aligned} \quad (31)$$

Using (31) and the solution of ODE (27), power spectral density (PSD) and, subsequently, SNR can be computed at frequency Ω_o of the input signal. The expression for SNR given by (32) reveals that for a particular value of σ , SNR

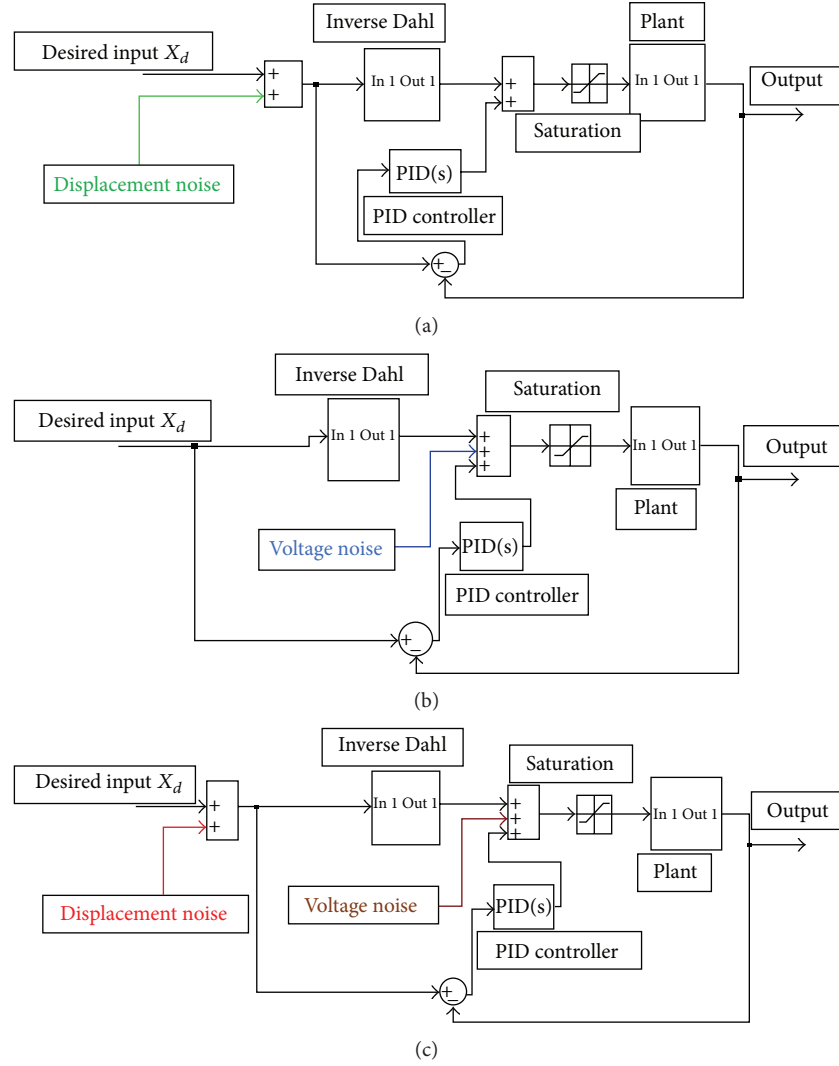


FIGURE 8: (a) Displacement dither control paradigm, (b) voltage dither control paradigm, and (c) combined dither paradigm.

attains a maximum and SR is manifested. Consider the following:

$$\text{SNR} = \frac{4\pi\lambda^2 A_o^2 \zeta^2 \delta(0)}{\sigma^4 (r_L^{-1} + r_r^{-1})} + o(\lambda^2). \quad (32)$$

3.3.3. SR in Piezoelectric-Stage Actuated Platform. The dynamics of PZA are encapsulated by (1). The operation of piezoelectric actuator demands operating it in close proximity to the sample on which the positioning has to be performed. For example, in AFM, the piezo tip is made to scan the sample while moving very close to the sample. Such interactions invariably engender long range attractive forces and short range repulsive forces acting on the piezo due to sample at distance Z . This force is given by (33) where Δ and θ are parameters depending upon the material of piezo tip and sample on which piezo is operating. The potential of piezoelectric-stack actuated platform operating inside the sample surface potential is described by (34) which clearly refers to an unsymmetrical bistable potential.

An illustration of this potential function with parameters set at the following values is shown in Figure 6: $K/M = 40$, $\theta = 0.26$, $\Delta = 0.05$, $Z = 0.5$,

$$F = -\frac{M\theta}{(x+Z)^2} + \frac{M\theta\Delta^6}{30(x+Z)^8}, \quad (33)$$

$$V(x) = \frac{K}{2M}x^2 - \frac{\theta}{(x+Z)} + \frac{\Delta^6\theta}{210(x+Z)^7}. \quad (34)$$

The amazing capability of dither induced SR can be utilized in the realm of PZAs in ameliorating hysteresis. However, an important issue to be addressed is the selection of a proper dither sequence and the mode of dither inoculation. Authors have investigated the effects of different dither sequences, namely, Rician, Rayleigh, and Sinusoidal and Gaussian dithers, and the results are presented in Figure 7. It was found that sinusoidal dither has the most linearizing capability and its generation mechanism is fairly simple. Because of these advantages, sinusoidal dither is selected for

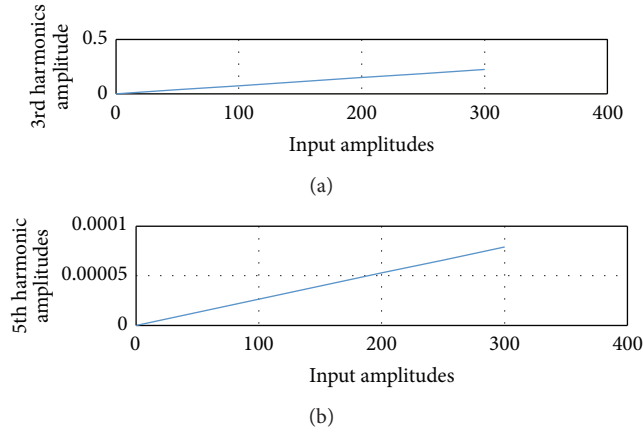


FIGURE 9: Curve fitting of the magnitudes of (a) 3rd harmonic amplitudes and (b) 5th harmonic amplitudes.

all further experimentations in this study. Three different dither inoculation modes have also been analyzed in [41, 42]. A brief description of these modes is presented here.

(a) *Displacement Dither Control Mode.* Noise is fed into the system along with the input trajectory to be tracked. Since this dither has dimensions the same as the input, that is, displacement, this control paradigm is termed as displacement dither control. The dither intensity is tuned to achieve the least tracking error. An illustration of this control is presented in Figure 8(a).

(b) *Voltage Dither Control Mode.* In this paradigm, the dither is inoculated as a voltage along with the compensated voltage through the inverse Dahl model as shown in Figure 8(b). Starting with arbitrary dither intensity, the best voltage dither is obtained for which tracking error is the least.

(c) *Combined Dither Control Mode.* This is a synergistic combination of the two aforementioned control schemes. Combined dither control as depicted in Figure 8(c) utilizes simultaneous dithering at both displacement and voltage points in the system. Both the dithers are tuned individually to yield the best plant performance.

3.4. Adaptive Dither Based Hysteresis Compensation. All real-time systems are subjected to uncertainties arising out of unmodeled system dynamics, parametric variations, disturbances, and process changes. In order to successfully compensate the impact of these uncertainties, a special class of controller is needed which is able to monitor the plant dynamics and can adjust its control law to compensate for the uncertainties. Such an adaptive controller is proposed here which can adjust the dither intensity adaptively and, hence, influences the control.

3.4.1. FFT Based Adaptive Dither Control (FFT-ADC). Hysteresis characterization based on observing the shape and size of hysteretic loops is not a well defined measure to quantify hysteresis. In order to obtain a true knowledge of the amount

of hysteresis present in PZA, it is necessary to develop a quantitative measure of the degree of hysteretic nonlinearity. This measure should meet the following two criteria:

- (a) it should be easy to derive;
- (b) it should be valid over a large range of operating conditions irrespective of drive amplitude and frequency.

One such measure is the spectral density of PZA output. The harmonics in output can be utilized to characterize hysteresis content of PZA. In an effort to establish a relationship between harmonics and hysteresis, frequency domain analysis of the actuator response becomes necessary. Hysteresis varies in direct proportion with the harmonic amplitudes. The greater the harmonic amplitudes in the spectral analysis, the higher the hysteretic nonlinearity in the PZA. To substantiate this claim, the variation of 3rd and 5th harmonics with varying input amplitudes is plotted in Figure 9. Clearly, both of these harmonics vary in direct proportion with the input amplitude. It is a well-known fact that hysteresis increases with an increase of input amplitude. In other words, an increase in input amplitude is characterized by an increase in hysteresis as well as harmonic amplitudes. An indirect relationship can thus be established between hysteresis and PZA output harmonic amplitudes. The output harmonics of PZA can now be selected as a metric to comment upon hysteresis in PZA. However, to quantify the amount of hysteresis, a mathematical formulation is necessary. Weak scalability of PZA substantiates the effort in quantifying hysteresis through a frequency based analysis.

(1) *Weak Scalability.* For a sinusoidal input with a fundamental frequency f , the fast Fourier transform (FFT) of PZA output can be expressed as a sum of fundamental frequency signal and other harmonics. The frequency information present in the output can be expressed in terms of fundamental frequency according to (35). The harmonic amplitude for $(2n + 1)$ th order harmonic is given by h_{2n+1} and harmonic ratio is defined by (36). A relative invariance of the harmonic ratio with a change in drive frequency is referred to as weak scalability:

$$f_i = (2n + 1) f, \quad \text{where } n = 0, 1, 2, 3 \dots, \quad (35)$$

$$d_{2n+1} = h_{2n+1} - h_{2n-1}. \quad (36)$$

The variation of 3rd and 5th harmonics in the output spectrum of PZA with different input amplitudes is plotted in Figures 9(a) and 9(b), respectively. Clearly, 3rd harmonic as well as 5th harmonic amplitudes are nearly linearly proportional to the input signal amplitude. Hysteresis varies in direct proportion to the input signal amplitude and increases with an increase of input amplitude. The low order harmonics have a predictable behavior and increase linearly with increase of input amplitude. This analogy between hysteresis and harmonics facilitates the development of a suitable harmonic based metric to quantify hysteresis. Such a variation of low order harmonics implies that the harmonic ratio d_{2n+1} remains almost constant within a certain range of input

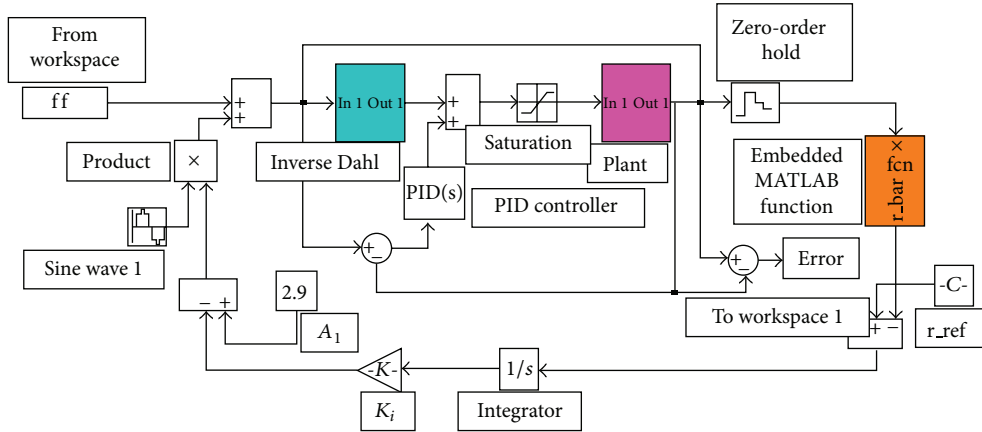


FIGURE 10: MATLAB/simulink representation of adaptive dither based FFT adaptive loop control.

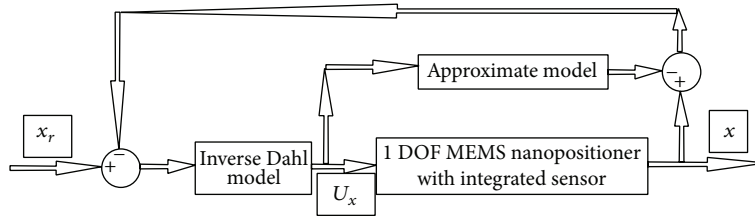


FIGURE 11: General schematic of internal model control employed with feedback.

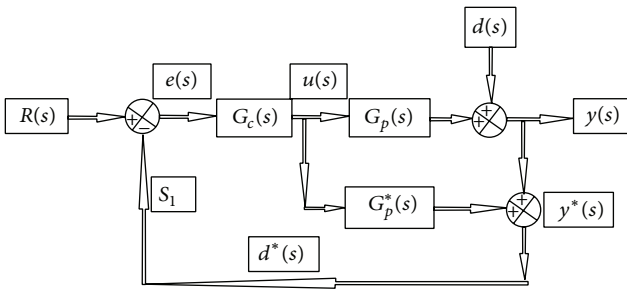


FIGURE 12: Basic structure of internal model control.



FIGURE 13: Experimental setup of the piezoactuator.

amplitude. This observation is corroborated by Table 1. With sinusoidal inputs (frequency 1 Hz) varying in a wide range from $10 \mu\text{m}$ to $300 \mu\text{m}$, the fluctuations in harmonic ratios are tabulated in Table 2. Evidently, the variations in d_3 , d_5 , and d_7

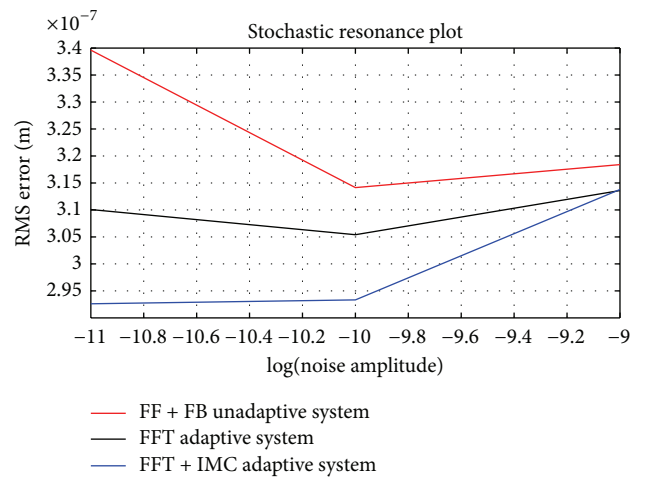


FIGURE 14: Stochastic resonance plots: tracking error versus noise intensity.

remain bounded within ± 0.8215 dB. This establishes that the PZA model considered here is weakly scalable.

(2) *Control Scheme.* The relationship between time domain hysteresis plots and frequency domain harmonic analysis validates the development of normalized harmonic ratio as measure of hysteresis quantification [46]. Let the normalized harmonic ratio be defined as

$$R_{(2n+1)f} = \frac{H_{(2n+1)f}}{H_f}, \quad (37)$$

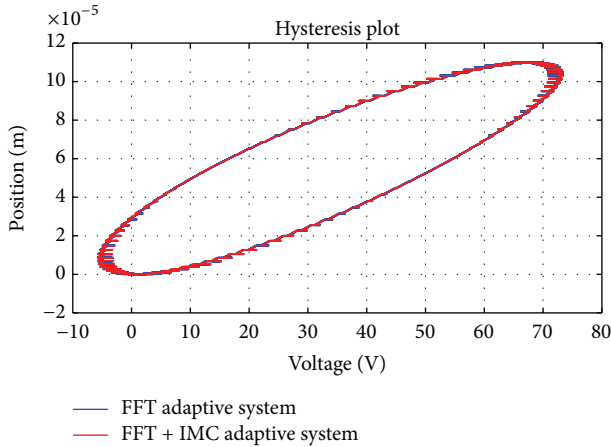


FIGURE 15: Hysteresis plots with adaptive controls.

TABLE 1: Variation of harmonic ratios with input variation.

A (μm)	d_3 (dB)	d_5 (dB)	d_7 (dB)
10	-8.377	-5.197	-2.977
20	-10.020	-4.408	-2.640
40	-9.140	-4.345	-2.960
80	-9.164	-4.359	-2.881
110	-9.164	-4.359	-2.881
150	-9.114	-4.365	-2.855
200	-9.117	-4.321	-2.915
300	-9.321	-4.342	-2.945

where $H_{(2n+1)f}$ is the amplitude of $(2n + 1)$ th harmonic and $n = 1, 2, 3, \dots$. Being weakly scalable, a change in the value of R represents a change in harmonic amplitude and, hence, a change in PZA hysteresis. To capture the effects of all the major harmonics present in the system output, a broader consideration of the normalized harmonic ratio is needed. To meet this end, the harmonic ratio for the whole system is defined as

$$\bar{R} = \sum_{n=1}^N \frac{R_{(2n+1)f}}{N}. \quad (38)$$

For instance, if $N = 3$, the normalized system harmonic ratio becomes

$$\bar{R} = \frac{R_3 + R_5 + R_7}{3} = \frac{H_3 + H_5 + H_7}{3H_1}, \quad (39)$$

where H_i is the amplitude of the i th order harmonic. For higher values of N , all other harmonics except 3rd, 5th, and 7th have insignificant amplitudes and thus R_9, R_{11}, \dots can be ignored without significant loss of generalization.

The capabilities of dithering have been seen to mitigate the effects of hysteretic nonlinearity significantly. To utilize the effects of dithering as well as the benefits of adaptive control, a dither based FFT adaptive Loop scheme has been developed here. This scheme uses normalized harmonic ratio (\bar{R}) as a suitable metric to indicate the amount of hysteretic

TABLE 2: Identified dynamic model parameters of the micromanipulator with Dahl hysteresis.

Parameter	Value	Unit
M	0.041	kg
D	13.53	N s/m
K	26.8×10^6	N/m
T	0.0108	C/m
a_1	386.854	—
a_2	2.315×10^6	—
b_1	1.021×10^6	—
b_0	0	—

nonlinearity. While in the displacement dithering mode the FFT of system output is calculated to compute \bar{R} . Although hysteresis smoothing by adaptive dither control is the objective of the proposed scheme, issues such as “what is a suitable dither amplitude?” and “what is a criterion of reduction of nonlinearity?” need to be addressed. The limiting condition for nonlinearity compensation is taken as the minimum condition which if present can restrict the system harmonic ratio \bar{R} less than a prespecified value. This is achieved by assigning a reference value \bar{R}_{ref} (assumed to be 10% of the value of \bar{R} for undithered system) and comparing the system harmonic ratio \bar{R} with the reference at every instant. This algorithm aims at restricting system harmonic nonlinearity within 10% of the nonlinearity observed with undithered system and hence can achieve a drastic improvement over undithered system. For undithered system, \bar{R} is found to be $1.81e(-14)$.

The other vital issue is the initial selection of best dither amplitude which will be used as the unadaptive part of dither. The dither amplitude chosen for experimentation is the same dither intensity which was adjudicated by the best displacement dither during unadaptive dither control. The adaptive algorithm for updating the effective dither amplitude during each sampling interval in accordance with \bar{R} is described below.

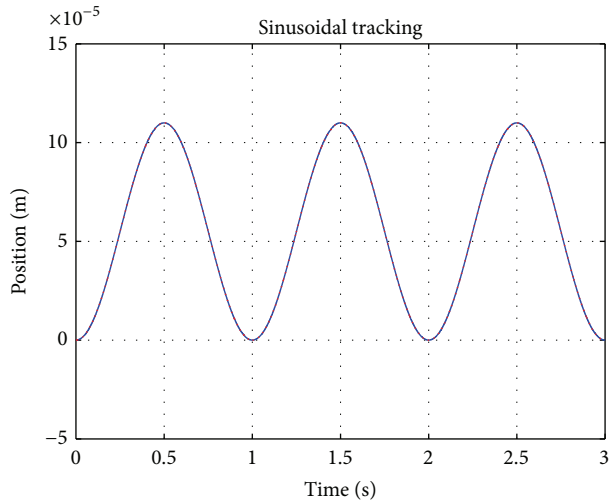
The normalized system harmonic ratio is compared with \bar{R}_{ref} to ensure the desired harmonic reduction. The error thus generated is worked upon by an integrator which sums up the error effect during each sampling interval. A_d is compared with constant A_1 to yield A :

$$e = \bar{R}_{\text{ref}} - \bar{R},$$

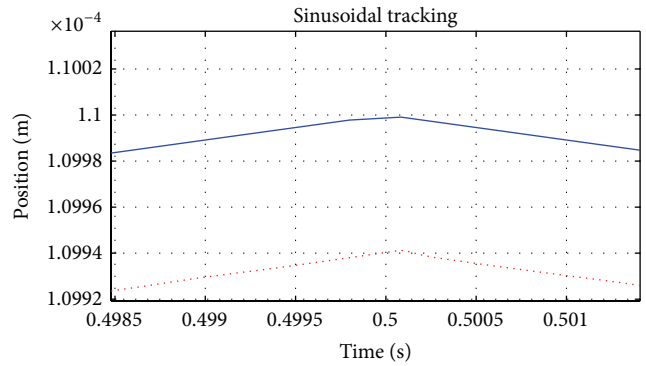
$$A_d = K_i \int_0^t e(t) dt, \quad (40)$$

$$A = A_1 - A_d.$$

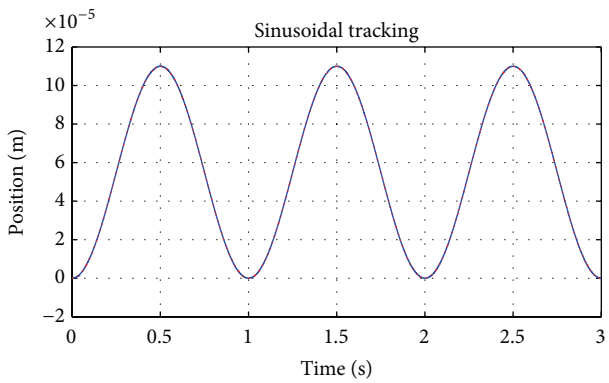
Here, A_1 is the initial best estimate of suitable dither amplitude and A_d is the compensated adaptively generated dither amplitude. The schematic of the closed loop FFT adaptive control is illustrated in Figure 10. To better illuminate the adaptive dither mechanism, let us assume an example. For instance, if the best voltage dither for unadapted system is found out to be $10e(-11)$, then the adapted part of dither



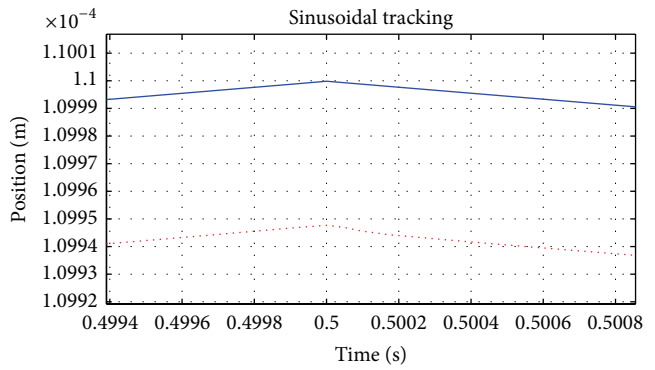
(a)



(b)

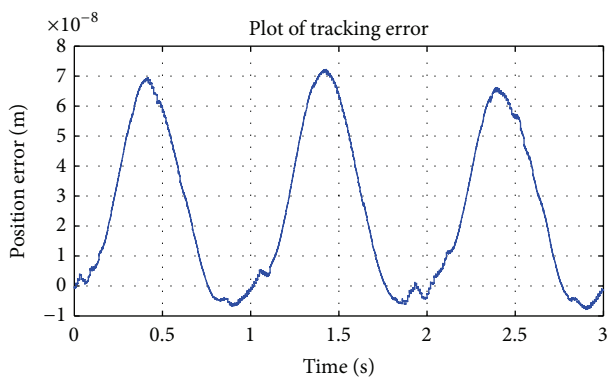


(c)

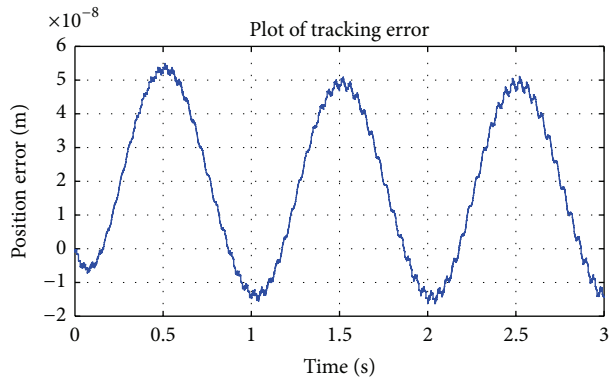


(d)

FIGURE 16: Sinusoidal signal tracking results: (a)-(b) undithered system and (c)-(d) FFT ADC system.



(a)



(b)

FIGURE 17: Tracking error plots for (a) undithered system and (b) FFT ADC system.

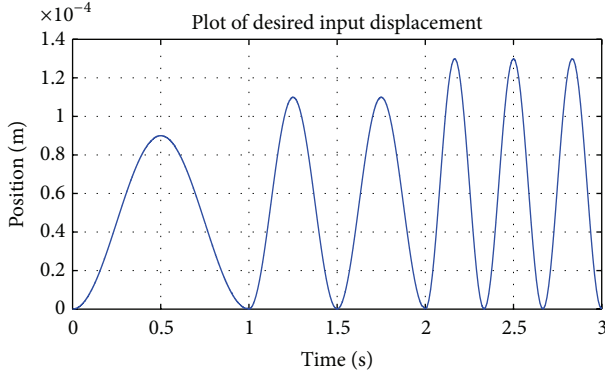


FIGURE 18: Multi-amplitude multifrequency input signal.

amplitude A is constrained to have a value between 1 and 10. If A goes beyond this range, then effective dither amplitude will change by a factor of 10. This will result in a greater error as effective dither amplitude is no longer equal to the best dither amplitude. A_1 is selected such that $A = A_1 - A_d$ complies with the needs of the adapted part. In our study, \bar{R}_{ref} is calculated to be $1.81e(-15)$ and A_1 is assigned a value of 2.9.

3.4.2. FFT Plus IMC Feedback Compensation (FFT-IMC). The previous subsection focused on the development of a frequency based adaptive control structure for 2-DOF nanopositioner. Adaptive tracking can successfully handle disturbances and parametric uncertainties, but it presupposes the knowledge of the entire trajectory to be tracked. This renders the adaptive scheme unsuitable for tracking unknown trajectories. This subsection introduces the design of an internal model control (IMC) based feedback controller for the adaptive system with the objective of imparting extra robustness to the system against the effects of external disturbances and parametric variations and to enhance unknown trajectory tracking accuracy. Rakotondrabe et al. have demonstrated that simple and robust controllers based on IMC feedback can efficiently reject cross-coupling effects and disturbances for piezoelectric micro/nanopositioning systems [47]. Furthermore, the computation and implementation of the controller is very simple.

(1) Control Mechanism. The philosophy underlying IMC states that if the trajectory to be tracked belongs to the set of all trajectories generated by a fixed dynamical system, then a perfect control is achievable in spite of endogenous or exogenous disturbances provided the controller incorporates an internal model of the system [48]. Unlike adaptive tracking control, IMC does not demand a complete knowledge of the past, present, and future time history of the trajectory being tracked.

The incorporation of an approximate model of the system is essentially the signature of IMC. Generally, IMC schemes place the approximate model in parallel to the process/plant. The general schematic of IMC employed in feedback is depicted in Figure 11. The feedback is constituted by comparing the approximate model output with the process output.

In the diagram, x_d is the reference input for the closed loop. The IMC closed loop is composed of an inverse plant model cascaded with an approximate plant model. Gaussian disturbance is added after the plant to realize the effect of unmodeled disturbances.

The basic structure of IMC is illustrated in Figure 12, where G_c is the IMC controller, G_p is the actual plant, G_p^* is process or plant model, d is the disturbance, and d^* is the estimated disturbance. Evidently, the manipulated input $u(s)$ is fed as input to both plant and process model. The error between the outputs of the two plants results in the signal $d^*(s)$. The feedback signal to the controller is given by

$$d^*(s) = [G_p(s) - G_p^*(s)] \cdot u(s) + d(s). \quad (41)$$

The error $E(s)$ takes into account process-model mismatch and other disturbances where

$$E(s) = R(s) - d^*(s). \quad (42)$$

The controller output $u(s)$ is obtained using the following formulation:

$$\begin{aligned} u(s) &= [R(s) - d^*(s)] \cdot G_c(s) \\ \implies u(s) &= [R(s) - \{[G_p(s) - G_p^*(s)] \cdot u(s) + d(s)\}] \\ &\quad \cdot G_c(s). \end{aligned} \quad (43)$$

Also,

$$u(s) = \frac{[R(s) - d(s)] \cdot G_c(s)}{1 + \{G_p(s) - G_p^*(s)\} G_c(s)}. \quad (44)$$

But

$$y(s) = G_p(s) \cdot u(s) + d(s). \quad (45)$$

In closed loop, the transfer function of the system yields

$$y(s) = \frac{\text{num}}{\text{den}}, \quad (46)$$

where

$$\begin{aligned} \text{num} &= \{G_c(s) \cdot G_p(s) \cdot r(s) + [1 - G_c(s) \cdot G_p^*(s)] \cdot d(s)\}, \\ \text{den} &= \{1 + [G_p(s) - G_p^*(s)] \cdot G_c(s)\}. \end{aligned} \quad (47)$$

If $G_c = G_p^{-1}$ and $G_p(s) = G_p^*(s)$, a perfect set point tracking and disturbance rejection can be achieved.

4. Results and Discussions

A preloaded piezoactuator with integrated feedback strain gauge sensor has been used which provides subnanometer resolution as well as sub millisecond response, for closed loop operation. A data acquisition system (cRIO-9073) is used to interface the equipment with LABVIEW real-time workshop. FPGA mode of cRIO-9073 is used which consists of an 8-slot

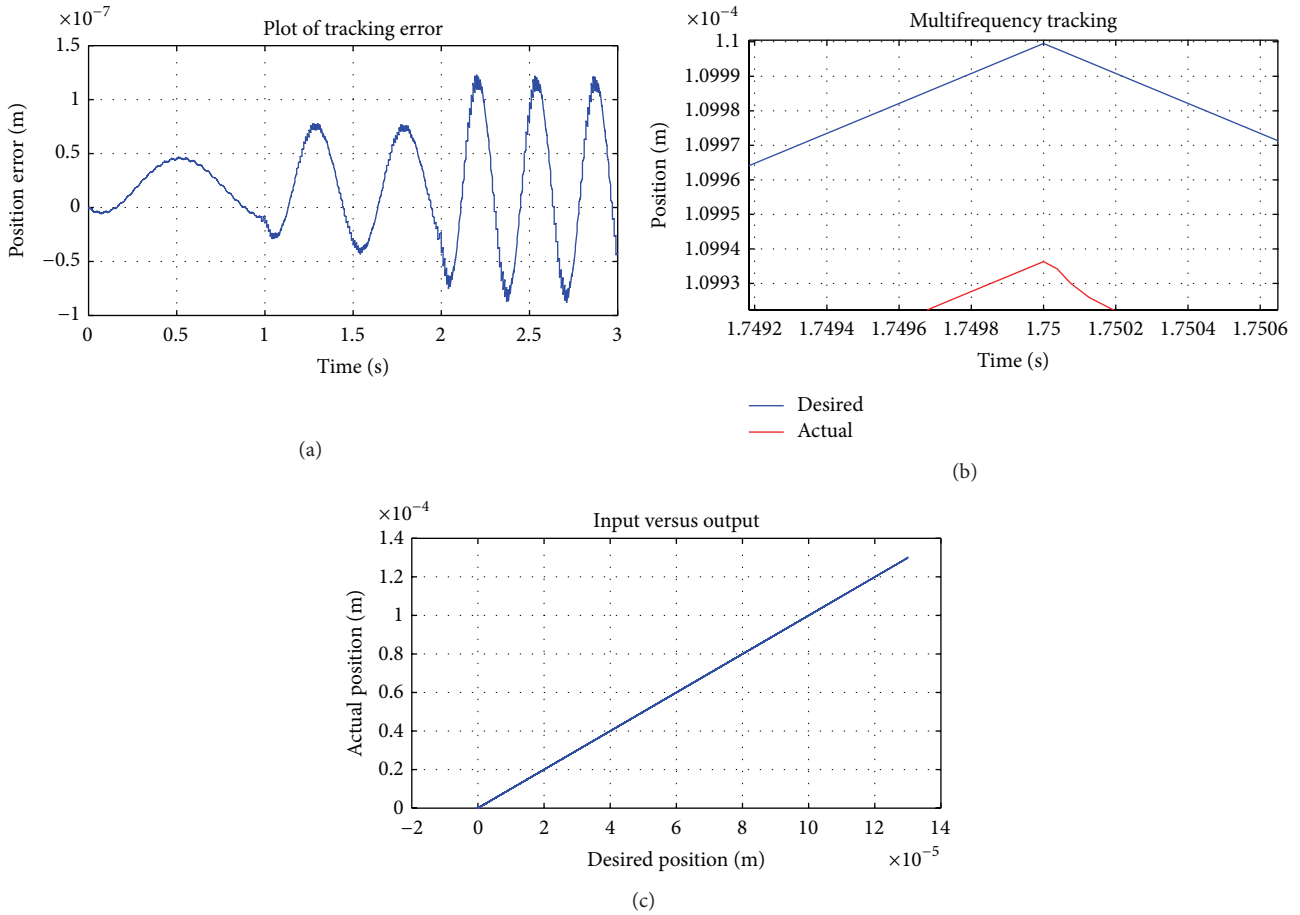


FIGURE 19: Multi-amplitude, multi-frequency tracking results of undithered system: (a) tracking error, (b) zoomed version of desired versus actual position, and (c) input versus output plot.

integrated 266 MHz real-time controller. cRIO is equipped with a 16-bit analog input module, a universal analog input module, and an analog output card. A schematic representation of the experimental setup is shown in Figure 13. The identified model parameters of the micro/nanomanipulator with Dahl model hysteresis are listed in Table 2.

Experiments were performed to demonstrate the efficacy of the proposed control structures for linearizing the effects of hysteresis. The natural frequency and the damping factor of the actuator can be calculated using the open loop step response of the actuator with a step input of 75 V. Following the flow outlined in [37], using the FFT of open loop step response, natural frequency of the actuator is calculated to be 145 Hz. The sampling frequency to be chosen for the experimentations depends on many factors [49]. Firstly, a sampling frequency at least ten times or larger than the natural oscillation frequency ensures system behavior is encapsulated precisely without introducing excessive noise. Second, the time constant of the system imposes an additional constraint that the sampling frequency should be not lower than $3/\tau$, where τ represents the system time constant. In view of these two factors, the sampling frequency is chosen as 8 kHz in the experimental tests.

4.1. Stochastic Resonance. To start with, the phenomenon of dither induced stochastic resonance is tested for. In unadaptive mode, the system is dithered in possible configurations, namely, displacement dithered, voltage dithered, and combined dithered. Starting with arbitrary dither intensity, the dither magnitude is varied in a wide range as shown in Figure 14. Clearly, for every control mode, the tracking error reaches a minimum for only specific dither intensity. On either side of this dither value, the tracking error increases. For unadaptive displacement dithering, stochastic resonance manifests itself for a dither intensity of $10e(-11)$. This value is set as the best dither value for FFT based adaptive dither control scheme as well. Similar observation for FFT based adaptive dither control (FFT-ADC) and FFT+IMC based adaptive dither control confirms the exhibition of stochastic resonance.

4.1.1. Sinusoidal Motion Tracking Test. In order to visualize hysteresis reduction, tracking error results for different controllers are compared in Table 3. FFT+IMC has a distinctly improved response as compared to undithered system with RMS tracking error reduced by 8.05 nm (see Figures 16 and 17). The output hysteresis loop also points to this fact,

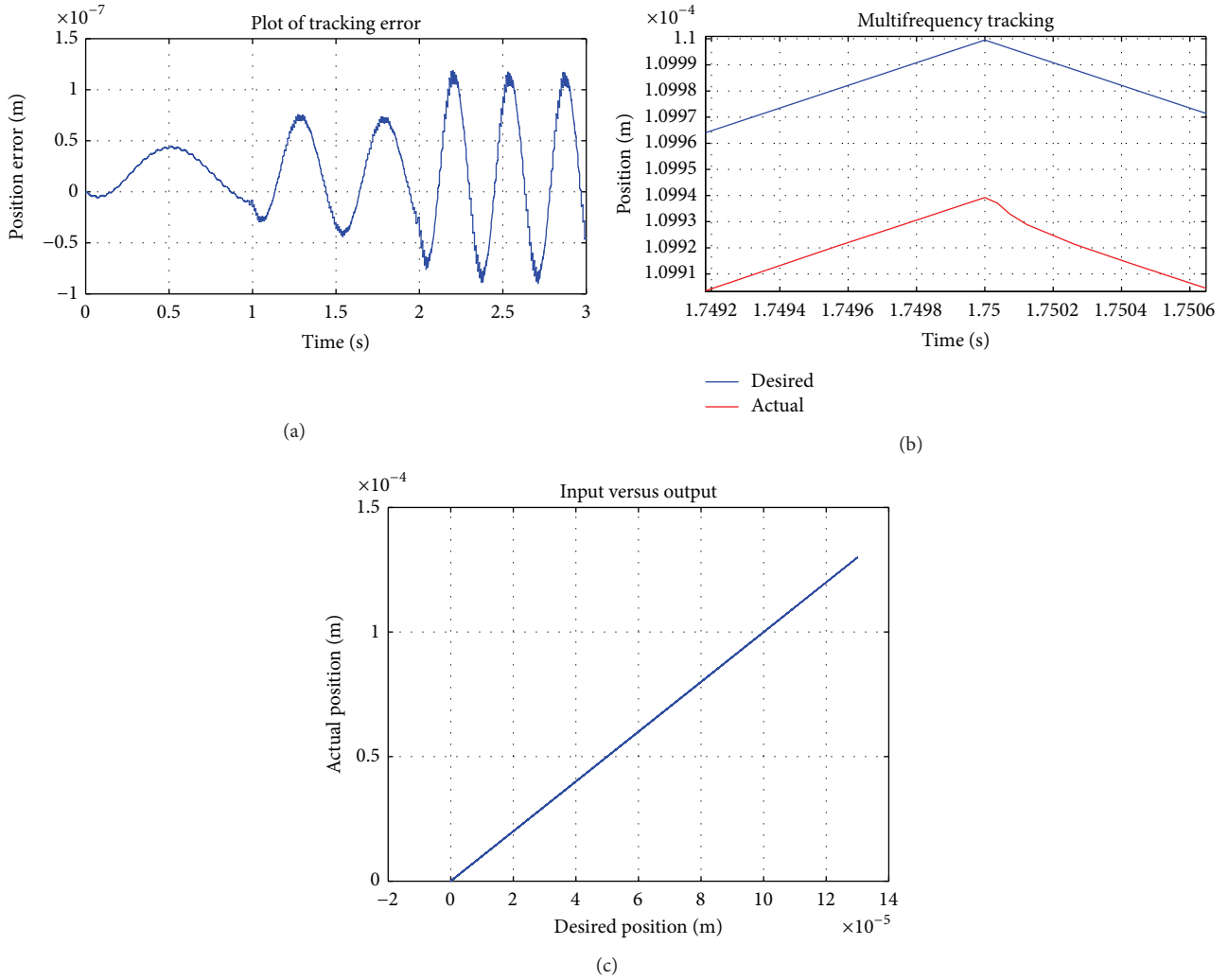


FIGURE 20: Multi-amplitude, multifrequency tracking results of FFT ADC system: (a) tracking error, (b) zoomed version of desired versus actual position, and (c) input versus output plot.

TABLE 3: Performance comparison of different control paradigms.

Type of control	RMS error (in nm)	% error reduction
Undithered system	37.311	0
Unadaptive best voltage dithered	35.83	3.969
Unadaptive best displacement dithered	31.42	15.788
Unadaptive best combined dithered	30.918	17.134
FFT adaptive dither control	30.541	18.144
FFT + IMC adaptive dither control	29.261	21.575

Figure 15 where maximum output hysteresis is 0.0266 percent of the total output range.

4.1.2. *Multi-amplitude, Multifrequency Tracking Test.* The system response to varying inputs is checked by multi-amplitude, multifrequency tracking. The PZA is simulated with an input shown in Figure 18 of amplitudes 90 μm , 110 μm , and

130 μm and corresponding frequencies of 1 Hz, 2 Hz, and 3 Hz, respectively. The tracking results in Figures 19 and 20 illustrate that FFT+IMC has a superior response to sudden changes in input amplitude/frequency. To the given input, the undithered system has an error of 65 nm while FFT+IMC reacts nearly smoothly with an error of only 60 nm.

4.1.3. *Circular Contour Tracking Test.* A spatial reference trajectory is applied to the positioner in order to verify its ability to track complex 2D trajectories. The inputs applied to the x - and y -axes is given as follows:

$$\begin{aligned} x_r(t) &= A \sin(2\pi f_r t), \\ y_r(t) &= A \sin(2\pi f_r t + \phi), \end{aligned} \tag{48}$$

where A is the amplitude in μm , f_r is the frequency of rotation of nanopositioner's stage, and ϕ is the phase angle difference between x - and y -axes inputs.

Figure 21 shows the results obtained with two axis tracking for the radii of 90 μm , 110 μm , and 130 μm , respectively,

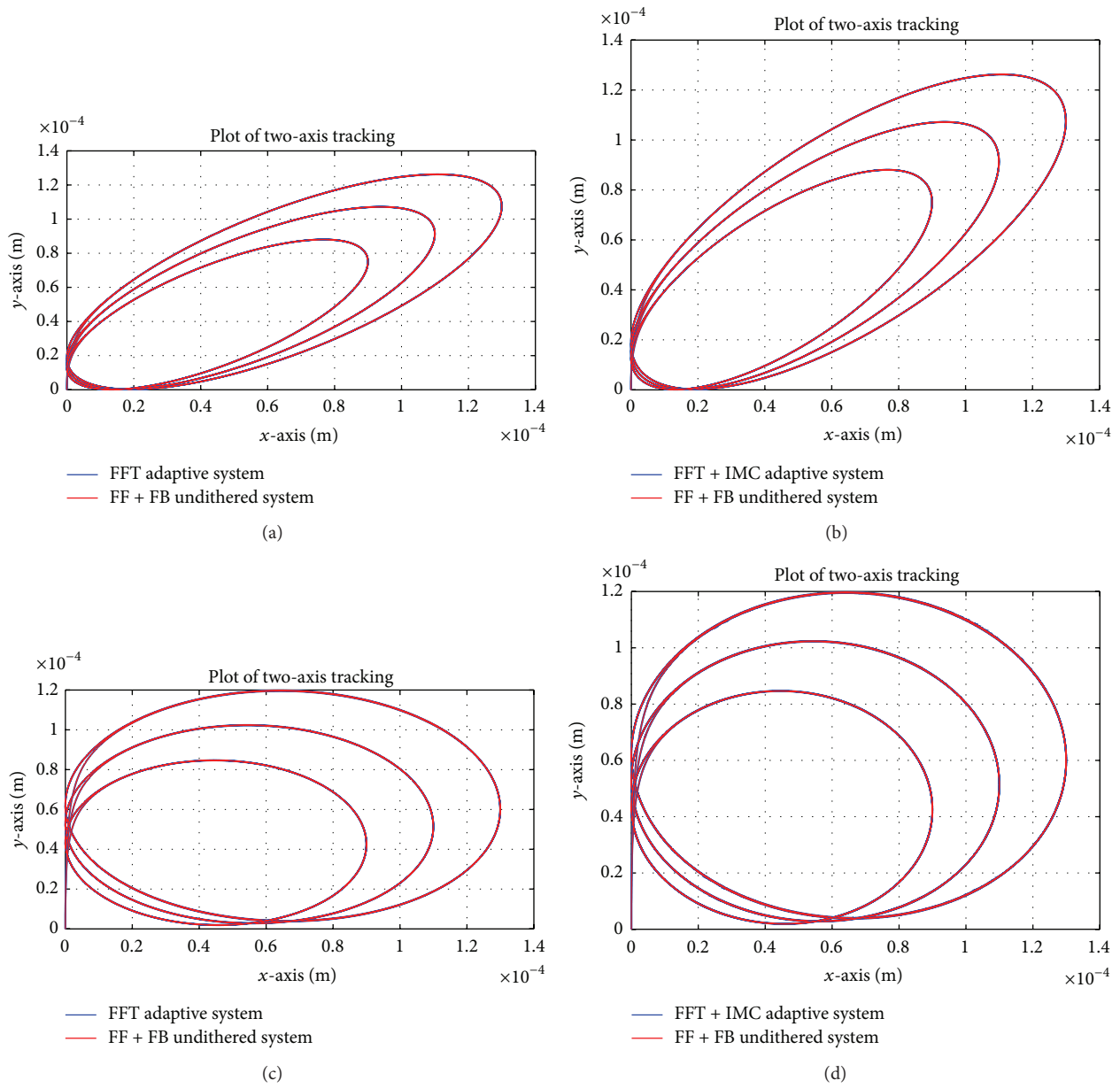


FIGURE 21: Circular contouring results with an input rate of 0.25 Hz and different amplitudes and the biaxial inputs differing by (a and b) phase angle of 45° and (c and d) phase angle of 90°.

TABLE 4: Two-dimensional RMS circular contouring errors of the XY parallel manipulator characterized with FFT ADC system.

Amplitude (in μm)	Frequency							
	0.25 Hz				0.5 Hz			
	60°		90°		60°		90°	
	SD (in μm)	RMS (in μm)	SD (in μm)	RMS (in μm)	SD (in μm)	RMS (in μm)	SD (in μm)	RMS (in μm)
90	1.6876	2.4099	3.1386	4.3457	2.8904	4.1973	3.6637	5.2480
110	2.1992	3.2913	4.0012	5.8561	2.9940	4.5504	4.2329	6.1214
130	2.7665	4.2916	4.9366	7.5628	3.2069	5.0194	4.9776	7.1812

TABLE 5: Two-dimensional RMS circular contouring errors of the XY parallel manipulator characterized with FFT + IMC system.

Amplitude (in μm)	Frequency							
	0.25 Hz				0.5 Hz			
	60°		90°		60°		90°	
	SD (in μm)	RMS (in μm)	SD (in μm)	RMS (in μm)	SD (in μm)	RMS (in μm)	SD (in μm)	RMS (in μm)
90	1.6870	2.4082	3.1382	4.3444	2.8907	4.1966	3.6637	5.2472
110	2.1983	3.2892	4.0007	5.8545	2.9940	4.5494	4.2325	6.1203
130	2.7655	4.2892	4.9359	7.5611	3.2066	5.0181	4.9769	7.1799

TABLE 6: RMS tracking error comparison between FF + FB system and FFT + IMC system for plant parametric variations.

	+2% variation		-2% variation		Variation range	
	FF + FB	FFT + IMC	FF + FB	FFT + IMC	FF + FB	FFT + IMC
Dynamic parameters						
M	31.911 nm	31.073 nm	29.896 nm	31.911 nm	2.015 nm	0.838 nm
D	362.97 nm	374.09 nm	405.81 nm	394.14 nm	42.84 nm	20.05 nm
K	1070.1 nm	1051.3 nm	1179.8 nm	1141.3 nm	109.7 nm	90 nm
T	1260 nm	1238.9 nm	1230.4 nm	1220.2 nm	29.6 nm	18.7 nm
Hysteretic parameters						
a_1	38.106 nm	31.577 nm	34.672 nm	29.365 nm	3.434 nm	2.212 nm
a_2	33.475 nm	30.406 nm	40.484 nm	30.193 nm	7.009 nm	0.213 nm
b_0	82.135 nm	94.582 nm	121.51 nm	108.73 nm	39.375 nm	14.23 nm
b_1	82.191 nm	77.489 nm	150.08 nm	134.38 nm	67.889 nm	56.891 nm

and each having a frequency 1 Hz. Besides, the input phase difference between the biaxial inputs is kept at 45° and 90°. A comparative analysis of FFT-ADC and FFT+IMC with regards to dual axis tracking is presented in Figure 21. The important observations for this test can be summarized as follows:

- (i) the contouring error increases with an increase in input amplitude;
- (ii) the tracking error aggravates for an increase of input frequency;
- (iii) increasing the phase difference between the biaxial inputs deteriorates system performance.

In Tables 4 and 5, SD and RMS represent standard deviation and root mean square of the tracking error, respectively. FFT+IMC brings about a significant linearization against hysteresis with maximum tracking error of only 7.5611 μm for an input trajectory given by

$$\begin{aligned} x_r(t) &= A \sin(2\pi f_r t), \\ y_r(t) &= A \sin(2\pi f_r t + 90^\circ). \end{aligned} \tag{49}$$

4.1.4. Parametric Sensitivity Test. To verify the robustness of IMC against parametric variations, parametric sensitivity test is undertaken. The results have been tabulated in Table 6. The parameters of the plant are varied in the range of $\pm 2\%$. It is seen that the plant output fluctuations are limited within

TABLE 7: Variation of tracking error with addition of process noise (at input).

Noise	FF + FB	FFT + IMC
$10e(-23)$	29.856 nm	31.723 nm
$10e(-24)$	36.812 nm	31.097 nm
$10e(-25)$	30.818 nm	31.687 nm
$10e(-26)$	37.692 nm	31.875 nm
$10e(-27)$	38.082 nm	30.604 nm
$10e(-28)$	37.733 nm	29.871 nm
$10e(-29)$	36.707 nm	30.32 nm
Variation range	7.877 nm	2.004 nm

90 nm with FFT-IMC when K is varied by $\pm 2\%$ from their nominal values. On the other hand, an undithered system registers severe output fluctuations (109 nm) with the same range of variation in K . Similarly, other parameters are varied individually and the results establish the robustness of FFT-IMC against parametric variations.

4.1.5. Robustness against External Disturbances. External noise is added to the system to determine proposed controller performance in the presence of noisy ambience. Table 8 indicates that when the measurement noise level is varied from $10e(-23)$ to $10e(-29)$, FFT-IMC based plant shows output fluctuations within 0.209 nm whereas the fluctuations

TABLE 8: Variation of tracking error with addition of measurement noise (sensor noise).

Noise	FF + FB	FFT + IMC
$10e(-28)$	37.052 nm	30.199 nm
$10e(-29)$	36.706 nm	30.235 nm
$10e(-30)$	37.913 nm	30.026 nm
$10e(-31)$	37.689 nm	30.163 nm
$10e(-32)$	36.753 nm	30.028 nm
Variation range	1.207 nm	0.209 nm

are much higher for undithered system at control mechanism (1.207 nm). Similar observation for process noise in Table 7 substantiates the robustness of FFT-IMC scheme over undithered system.

5. Conclusions

This paper presented a novel control structure aimed at mitigating the effects of hysteresis in a dual axis micro/nano-positioning stage. An inversion based feedforward approach cascaded with a feedback controller is seen to linearize hysteresis effectively. This control when augmented with dithering induces stochastic resonance which enhances the positioning accuracy of the stage for a specific dither input. However, a real-time implementation of these schemes demand for adaptive dither tuning ability. In order to achieve this end, a harmonic ratio based adaptive scheme called FFT-ADC is deployed. This control not only improves positional accuracy with hysteresis reduced by 0.0277% as compared to undithered system but also brings about the advantages of adaptive control.

To account for unmodeled systems dynamics and to impart added robustness against external disturbances and parametric variations, FFT-ADC is augmented with an IMC based feedback loop. FFT-IMC is seen to impart substantial inertness to the system with considerably reduced output fluctuations in presence of external noise and parametric variations. The experimental results have demonstrated the efficacy of the proposed control schemes, thus allowing for a better system response and an improved capability of disturbance rejection.

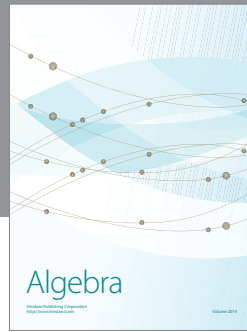
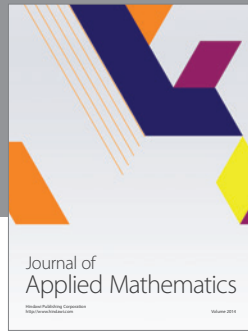
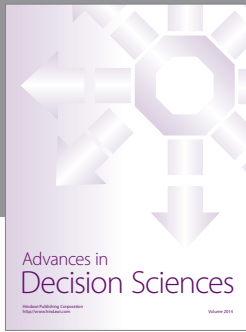
Conflict of Interests

The authors declare that there is no conflict of interests regarding the publication of this paper.

References

- [1] K. K. Leang, Q. Zou, and S. Devasia, "Feedforward control of piezoactuators in atomic force microscope systems," *IEEE Control Systems Magazine*, vol. 29, no. 1, pp. 70–82, 2009.
- [2] S. Bashash and N. Jalili, "Robust adaptive control of coupled parallel piezo-flexural nanopositioning stages," *IEEE/ASME Transactions on Mechatronics*, vol. 14, no. 1, pp. 11–20, 2009.
- [3] J. E. Colgate and N. Hogan, "Robust control of dynamically interacting systems," *International Journal of Control*, vol. 48, no. 1, pp. 65–88, 1988.
- [4] N. Hogan, "Impedance control: an approach to manipulation: part III—applications," *ASME Journal of Dynamic Systems, Measurement, and Control*, vol. 107, no. 1, pp. 17–24, 1985.
- [5] M. H. Raibert and J. J. Craig, "Hybrid position/force control of manipulators," *ASME Journal of Dynamic Systems, Measurement and Control*, vol. 103, no. 2, pp. 126–133, 1981.
- [6] H. Chaoui, P. Sicard, and M. Sawan, "High precision ANN-based adaptive displacement tracking of piezoelectric actuators for MEMS," in *Proceedings of the 8th IEEE International NEW-CAS Conference (NEWCAS '10)*, pp. 85–88, Montreal, Canada, June 2010.
- [7] J. Yi, S. Chang, and Y. Shen, "Disturbance-observer-based hysteresis compensation for piezoelectric actuators," *IEEE/ASME Transactions on Mechatronics*, vol. 14, no. 4, pp. 456–464, 2009.
- [8] G. Schitter, P. Menold, H. F. Knapp, F. Allgöwer, and A. Stemmer, "High performance feedback for fast scanning atomic force microscopes," *Review of Scientific Instruments*, vol. 72, no. 8, pp. 3320–3327, 2001.
- [9] S. Salapaka, A. Sebastian, J. P. Cleveland, and M. V. Salapaka, "High bandwidth nano-positioner: a robust control approach," *Review of Scientific Instruments*, vol. 73, no. 9, pp. 3232–3241, 2002.
- [10] D. Croft and S. Devasia, "Vibration compensation for high speed scanning tunneling microscopy," *Review of Scientific Instruments*, vol. 70, no. 12, pp. 4600–4605, 1999.
- [11] R. C. Smith, M. V. Salapaka, A. Hatch, J. Smith, and T. De, "Model development and inverse compensator design for high speed nanopositioning," in *Proceedings of the 41st IEEE Conference on Decision and Control*, pp. 3652–3657, December 2002.
- [12] T. Orłowska-Kowalska, M. Kamiński, and K. Szabat, "Implementation of a sliding-mode controller with an integral function and fuzzy gain value for the electrical drive with an elastic joint," *IEEE Transactions on Industrial Electronics*, vol. 57, no. 4, pp. 1309–1317, 2010.
- [13] Y. Li and Q. Xu, "Adaptive sliding mode control with perturbation estimation and PID sliding surface for motion tracking of a piezo-driven micromanipulator," *IEEE Transactions on Control Systems Technology*, vol. 18, no. 4, pp. 798–810, 2010.
- [14] H. C. Liaw, B. Shirinzadeh, and J. Smith, "Sliding-mode enhanced adaptive motion tracking control of piezoelectric actuation systems for micro/nano manipulation," *IEEE Transactions on Control Systems Technology*, vol. 16, no. 4, pp. 826–833, 2008.
- [15] X.-G. Yan, S. K. Spurgeon, and C. Edwards, "Memoryless static output feedback sliding mode control for nonlinear systems with delayed disturbances," *IEEE Transactions on Automatic Control*, vol. 59, no. 7, pp. 1906–1912, 2014.
- [16] X.-G. Yan, S. K. Spurgeon, and C. Edwards, "State and parameter estimation for nonlinear delay systems using sliding mode techniques," *IEEE Transactions on Automatic Control*, vol. 58, no. 4, pp. 1023–1029, 2013.
- [17] J. J. Slotine and S. S. Sastry, "Tracking control of nonlinear systems using sliding surfaces, with application to robot manipulators," *International Journal of Control*, vol. 38, no. 2, pp. 465–492, 1983.
- [18] H. Elmali and N. Olgac, "Sliding mode control with perturbation estimation (SMCPE): a new approach," *International Journal of Control*, vol. 56, no. 4, pp. 923–941, 1992.

- [19] A. J. Mehta, B. Bandyopadhyay, and A. Inoue, "Reduced-order observer design for servo system using duality to discrete-time sliding-surface design," *IEEE Transactions on Industrial Electronics*, vol. 57, no. 11, pp. 3793–3800, 2010.
- [20] B. Veselic, B. Perunicic-Drazanovic, and Č. Milosavljevic, "Improved discrete-time sliding-mode position control using Euler velocity estimation," *IEEE Transactions on Industrial Electronics*, vol. 57, no. 11, pp. 3840–3847, 2010.
- [21] C.-L. Hwang and Y.-M. Chen, "Discrete sliding-mode tracking control of high-displacement piezoelectric actuator systems," *Journal of Dynamic Systems, Measurement and Control*, vol. 126, no. 4, pp. 721–731, 2004.
- [22] G. Tao and P. V. Kokotovic, "Adaptive control of plants with unknown hystereses," *IEEE Transactions on Automatic Control*, vol. 40, no. 2, pp. 200–212, 1995.
- [23] X. Tan and H. K. Khalil, "Two-time-scale averaging of systems involving operators and its application to adaptive control of hysteretic systems," in *Proceedings of the American Control Conference (ACC '09)*, pp. 4476–4481, June 2009.
- [24] D. Croft, G. Shed, and S. Devasia, "Creep, hysteresis, and vibration compensation for piezoactuators: atomic force microscopy application," *Journal of Dynamic Systems, Measurement and Control*, vol. 123, no. 1, pp. 35–43, 2001.
- [25] D. Croft and S. Devasia, "Hysteresis and vibration compensation for piezoactuators," *Journal of Guidance, Control, and Dynamics*, vol. 21, no. 5, pp. 710–717, 1998.
- [26] G. Schitter and A. Stemmer, "Model-based signal conditioning for high-speed atomic force and friction force microscopy," *Microelectronic Engineering*, vol. 67–68, pp. 938–944, 2003.
- [27] Y. Zhao and S. Jayasuriya, "Feedforward controllers and tracking accuracy in the presence of plant uncertainties," *Journal of Dynamic Systems, Measurement and Control, Transactions of the ASME*, vol. 117, no. 4, pp. 490–495, 1995.
- [28] D. E. Rivera, M. Morari, and S. Skogestad, "Internal model control: PID controller design," *Industrial & Engineering Chemistry Process Design and Development*, vol. 25, no. 1, pp. 252–265, 1986.
- [29] C. E. Garcia and M. Morari, "Internal model control. A unifying review and some new results," *Industrial & Engineering Chemistry, Process Design and Development*, vol. 21, no. 2, pp. 308–323, 1982.
- [30] D. Ha, R.-Y. Kim, and D. Hyun, "Internal-model-principle-based robust optimal nonlinear control for position tracking of permanent-magnet synchronous motor servo system," *Transactions of the Institute of Measurement and Control*, 2014.
- [31] G. Song, J. Zhao, X. Zhou, and J. A. de Abreu-García, "Tracking control of a piezoceramic actuator with hysteresis compensation using inverse Preisach model," *IEEE/ASME Transactions on Mechatronics*, vol. 10, no. 2, pp. 198–209, 2005.
- [32] J.-C. Shen, W.-Y. Jywe, H.-K. Chiang, and Y.-L. Shu, "Precision tracking control of a piezoelectric-actuated system," *Precision Engineering*, vol. 32, no. 2, pp. 71–78, 2008.
- [33] S. Bashash and N. Jalili, "Robust multiple frequency trajectory tracking control of piezoelectrically driven micro/nano-positioning systems," *IEEE Transactions on Control Systems Technology*, vol. 15, no. 5, pp. 867–878, 2007.
- [34] C.-J. Lin and S.-R. Yang, "Precise positioning of piezo-actuated stages using hysteresis-observer based control," *Mechatronics*, vol. 16, no. 7, pp. 417–426, 2006.
- [35] S. K. Shome, M. Prakash, A. Mukherjee, and U. Datta, "Dither control for Dahl model based hysteresis compensation," in *Proceedings of the IEEE International Conference on Signal Processing, Computing and Control (ISPCC '13)*, pp. 1–6, September 2013.
- [36] S. K. Shome, S. Pradhan, A. Mukherjee, and U. Datta, "Dither based precise position control of piezo actuated micro-nano manipulator," in *Proceedings of the 39th Annual Conference of the IEEE Industrial Electronics Society (IECON '13)*, pp. 3486–3491, November 2013.
- [37] Q. Xu and Y. Li, "Dahl model-based hysteresis compensation and precise positioning control of an XY parallel micromanipulator with piezoelectric actuation," *Journal of Dynamic Systems, Measurement and Control, Transactions of the ASME*, vol. 132, no. 4, pp. 1–12, 2010.
- [38] D. Helmick and W. Messner, "Higher order modeling of hysteresis in disk drive actuators," in *Proceedings of the 42nd IEEE Conference on Decision and Control*, pp. 3712–3716, December 2003.
- [39] M. Clerc and J. Kennedy, "The particle swarm-explosion, stability, and convergence in a multidimensional complex space," *IEEE Transactions on Evolutionary Computation*, vol. 6, no. 1, pp. 58–73, 2002.
- [40] Q. Xu and Y. Li, "Error analysis and optimal design of a class of translational parallel kinematic machine using particle swarm optimization," *Robotica*, vol. 27, no. 1, pp. 67–78, 2009.
- [41] M. Prakash, S. K. Shome, S. Pradhan, and M. K. Patel, "A comparison of dithers for hysteresis alleviation in second order dahl model based piezoelectric actuator," in *Proceedings of the IEEE International Conference on Control, Automation, Robotics and Embedded System*, pp. 1–6, 2013.
- [42] S. Pradhan, S. K. Shome, M. Prakash, and M. K. Patel, "Performance evaluation of dither distributions of piezo electric actuators for nano-positioning," in *Proceedings of the IEEE International Conference on Control, Automation, Robotics and Embedded Systems (CARE '13)*, pp. 1–6, December 2013.
- [43] L. Gammaitoni, "Stochastic resonance in multi-threshold systems," *Physics Letters A*, vol. 208, no. 4–6, pp. 315–322, 1995.
- [44] L. Gammaitoni, P. Hänggi, P. Jung, and F. Marchesoni, "Stochastic resonance," *Reviews of Modern Physics*, vol. 70, no. 1, pp. 223–287, 1998.
- [45] M. Basso, M. Dahleh, I. Mezic, and M. V. Salapaka, "Stochastic resonance in AFM's," in *Proceedings of the American Control Conference (ACC '99)*, vol. 6, pp. 3774–3778, June 1999.
- [46] T. Hong and T. N. Chang, "Control of nonlinear piezoelectric stack using adaptive dither," in *Proceedings of the American Control Conference*, pp. 76–80, June 1995.
- [47] M. Rakotondrabe, A. G. Fowler, and S. O. Reza Moheimani, "Control of a novel 2-DoF MEMS nanopositioner with electrothermal actuation and sensing," *IEEE Transactions on Control Systems Technology*, vol. 22, no. 4, pp. 1486–1497, 2013.
- [48] A. Isidori, L. Marconi, and A. Serrani, *Robust Autonomous Guidance: An Internal Model Approach*, vol. 16, Springer, 2003.
- [49] Y. Zhu, *Multivariable System Identification for Process Control*, Elsevier, New York, NY, USA, 2001.



Hindawi

Submit your manuscripts at
<http://www.hindawi.com>

